Predictive Thermodynamic Model for Intrusion of Electrolyte Aqueous Solutions in Nanoporous Materials

Ambroise de Izarra, François-Xavier Coudert, Alain Fuchs, Anne Boutin

Predictive Thermodynamic Model for Intrusion of Electrolyte Aqueous Solutions in Nanoporous Materials

Ambroise de Izarra,[†,‡] François-Xavier Coudert,[*,‡] Alain H. Fuchs,[‡] and Anne Boutin[*,†]

†*PASTEUR, Département de Chimie, École Normale Supérieure, PSL University, Sorbonne Université, CNRS, 75005, Paris, France*

‡*Chimie ParisTech, PSL University, CNRS, Institut de Recherche de Chimie Paris, 75005 Paris, France*

E-mail: fx.coudert@chimieparistech.psl.eu; anne.boutin@ens.psl.eu

Abstract

We performed Monte Carlo simulations in the osmotic ensemble in three representative hypothetical pure-silica zeolites that are silicalite-1, chabazite and faujasite for which adsorption isotherm of water has been calculated from grand canonical Monte Carlo simulations. Monte Carlo moves in the osmotic ensemble to insert electrolyte reveal that ions do not penetrate the zeosils at water intrusion pressure because they are better solvated in the bulk for low-diameter pore zeosils, which is associated to a lower ion solvation. Then, Chemical potential of water in electrolyte solutions has been calculated and highlight the same dependency in pressure as the chemical potential of pure water. From these conclusions, we propose a thermodynamic model that revisit the law of osmotic pressure in order to predict the intrusion pressure in zeosils taking account of the nature of electrolytes in solution.

Introduction

One of the most important challenge of material science consists in the elaboration of devices that can efficiently generate, store and transfer energy. In particular, intrusion and extrusion of a non-wetting liquid in porous lyophobic systems is a promising technology investigated first by Eroshenko and co-workers,[1–8] where the non-wetting liquid penetrates the pores under high pressure, resulting in conversion of mechanical energy into fluid-solid interface energy. When the pressure is released, the mechanical energy can be restored upon release of the fluid. Historically, intrusion of water in pure-silica zeolites (also called "zeosils") has been first reported in 2001[9] and represents the starting point of subsequent intrusion and extrusion experiments performed on various zeosils.[10–19] Later, Tzanis and co-workers[20] discovered that replacing water by electrolyte solutions was an effective way to increase mechanical energy stored in zeosils, because of the shift of intrusion pressure towards higher values. For instance, it was shown that intrusion of highly concentrated LiCl solution ($\sim$ 20 M) in silicalite-1 increases intrusion pressure from 96 MPa to 280 MPa, resulting in an increase of

stored energy from 10 J/g to 31 J/g. Since this pioneering work, the nature and concentration of electrolyte on the intrusion and extrusion pressure and energetic properties of zeosils has been widely investigated.[21–37] In addition to zeosils, that are the scope of this work, we note that intrusion and extrusion of pure water and electrolyte solutions have also been investigated in other microporous materials, such as metal-organic frameworks ZIF-8,[38–41] ZIF-71[42] and other ZIF materials,[43–47] as well as MAF-6.[48]

Although the mechanism of water intrusion in hydrophobic microporous materials has been highlighted by Grand Canonical Monte Carlo (GCMC) simulations,[12,49,50] the mechanism of electrolyte intrusion is still under debate: it is characterized by an increase of intrusion pressure that depends both on electrolyte nature and concentration. Several hypotheses have been proposed such as ion desolvation,[20] osmotic effect,[41] confinement effect[51,52] or increase of solid-liquid interfacial tension.[53,54] Recently, it has been shown that intrusion of NaCl electrolyte solution in chabazite and LTA-type zeosils occurs in two steps.[21,30] First, only water molecules penetrate into the nanocages at respectively 44 and 36 MPa in chabazite and LTA-type zeosils. Then, ions penetrate at a much higher pressure of respectively 260 MPa and 140–240 MPa. This is supported by previous MC simulations performed by Zamfir and co-workers[54] where NaCl electrolyte penetrates a two-dimensional planar hydrophobic nanopores once water has been intruded inside it. The initial step consisting of intrusion of only water molecules is crucial for energy storage applications. Thus, the dependence of the intrusion pressure with the nature and concentration of electrolyte requires further investigation, which is the object of this work by relying on our recent implementation of molecular simulations with an osmostat for electrolyte aqueous solution.[55] Briefly, the osmostat is based on a hybrid Monte Carlo move using nonequilibrium molecular dynamics, named *Nonequilibrium Candidate Monte Carlo* (NCMC), proposed by Nilmeier[56] and later applied by Ross and co-workers[57] to sample the distribution of NaCl electrolyte around biomolecules. We previously calculated the chemical potential of ion exchange $\Delta\mu_{C_nA_m}(P)$ in the semi-grand canonical ensemble for "alchemically" transforming $(n+m)$ water molecules chosen randomly

into an electrolyte unit C_nA_m (where C^{m+} and A^{n-} denote respectively the cation and the anion electrolyte) in bulk electrolyte solution at fixed concentration. We used a modified version of the Widom insertion method except that the work performed during the alchemical transformation $W_{(n+m)H_2O \to C_nA_m}$ (refered as the "alchemical work" to be noted $W_{C_nA_m}$) is taken into account, instead of the difference of energy between the initial and final step of the alchemical transformation. This chemical potential used in combination with NCMC moves to insert or delete ions at constant number of particles in the system defines the osmotic ensemble, where the fictitious reservoir is an electrolyte solution at a concentration imposed by the chemical potential.

In this work, we investigated the intrusion of electrolyte solutions in three representative hypothetical zeosils (silicalite-1, chabazite and faujasite) chosen for their increasing channel/cage diameter and the availability of experimental data.[58] First, we calculated the isotherm of pure water intrusion by GCMC simulation in each of these three zeosils. Then, using the configurations of water-loaded zeolites at equilibrium at different pressures, we apply our osmostat[55] and found that the alchemical work associated with ion insertion in the zeosils is much lower than in the bulk, leading to very low probabilities of intrusion. Assuming that water penetrates first the porous materials as observed experimentally for chabazite and LTA-type zeosils,[21,30] we then revisited the law of osmotic pressure and derived an analytical model to predict intrusion pressure of electrolyte solutions in zeosils for various electrolyte and concentration.

Model and Methods

Systems and force field

The systems we studied are three representative pure silica zeolites: silicalite-1 (MFI topology), chabazite (CHA topology) and faujasite (FAU topology). For channel-type zeosil such as silicalite-1, the intrusion pressure of water depends on the channel diameter d_{ch} while for

cage-like zeosils (chabazite and faujasite), it correlates with the cage diameter d_{ca}.[36] We have chosen these zeosils because of the increasing "characteristic diameter": in increasing order, silicalite-1 (d_{ch} = 5.40 Å), chabazite (d_{ca} = 7.37 Å) and faujasite (d_{ca} = 11.24 Å).[59] The zeosils are generally considered rigid and it is assumed that no structural or chemical changes occur upon electrolyte intrusion or extrusion. We used the crystal structure determined by Olson[60] for silicalite-1, the chabazite structure is that reported by Calligaris[61] while faujasite structure is that published by Hriljac.[62]

Table 1: Cell parameters of zeosils used in this work.

	a (Å)	b (Å)	c (Å)	α (°)	β (°)	γ (°)
silicalite-1[60]	20.070	19.920	13.420	90	90	90
chabazite[61]	9.459	9.459	9.459	94.07	94.07	94.07
faujasite[62]	24.258	24.258	24.258	90	90	90

We note here that pure-silica faujasite has not been synthesized so far, and even experimental faujasites with high Si:Al ratios exhibit a significant number of aluminium atoms. The pure-silica faujasite used in this work is thus a speculative model based on the atomic coordinates that correspond to crystallographic data for a faujasite with a Si:Al ratio of 2.61. These unit cell parameters of the structures are given in Table 1, and their structures are represented in Figure 1. In this study, we simulated respectively a box of four, twelve and one unit cells for silicalite-1, chabazite and faujasite in order to have large enough systems to avoid side effects due to applications of periodic boundary conditions.

We chose the force field developed for silicalite-1 by Desbiens and co-workers[49] to model interactions for zeosils in this study. This force field is tailored to reproduce intrusion pressure of TIP4P water around $\sim$ 100 MPa, as observed in experiments.[63] Water molecules are modeled with the rigid TIP4P model[64] and the electrolytes are represented as charged beads that differs by their Lennard-Jones parameters and charges. We considered the following monovalent electrolytes which are: LiCl, NaCl, KCl, RbCl, CsCl, KF, KBr and KI. We also explored the following divalent electrolytes to probe influence of charge ion: $MgCl_2$, $CaCl_2$, $SrCl_2$ and $BaCl_2$. The details of the force field are given in Tables S1 to S4.[65,66]

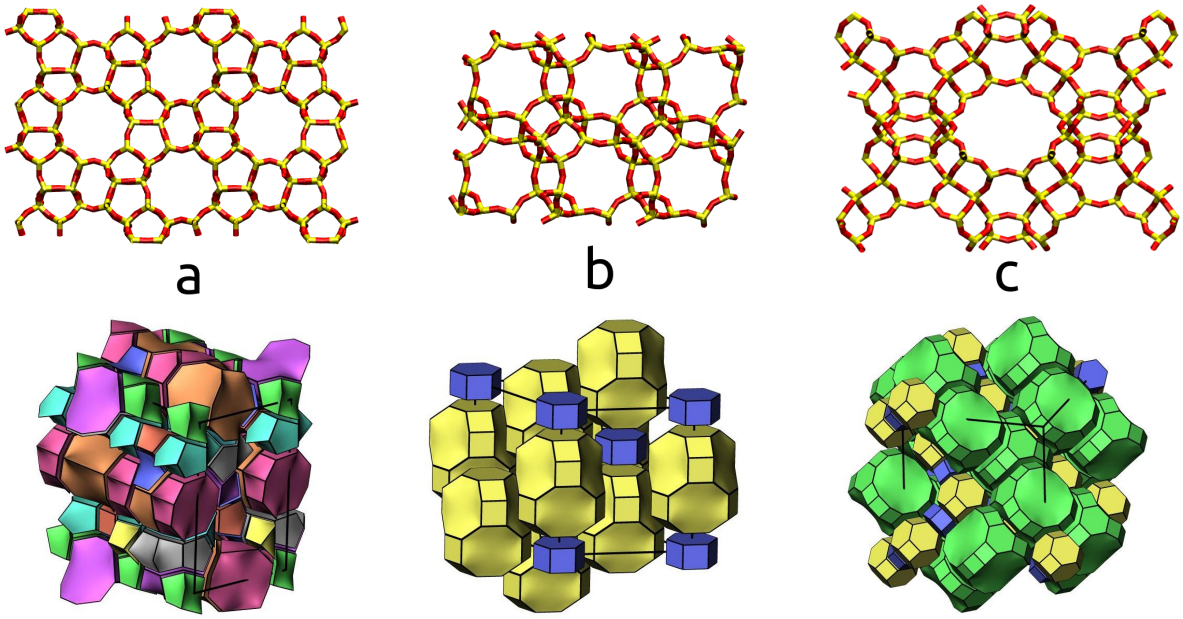

Figure 1: a) View of four unit cells of silicalite-1 along the crystallographic b axis. b) View of twelve unit cells of chabazite along the crystallographic b axis. c) View of one unit cell of faujasite along the crystallographic (1 1 0) direction. Bottom: the three corresponding tilings of the zeolite nets.

We used Lorentz–Berthelot mixing rules for cross-terms in Lennard-Jones potential, and Ewald summation to account efficiently for electrostatic interactions. We used a cutoff of 8.0 Å for both the Lennard-Jones potential and the separation between real space and reciprocal space in the Ewald summation.

Monte Carlo Simulations

Adsorption isotherms of pure water in zeosils were computed with GCMC simulations using the RASPA simulation package.[67] We screened several values of the chemical potential of the fictitious water reservoir[49] to compute the number of adsorbed water molecules by using the relationship between chemical potential of water and hydrostatic pressure $\mu_{\text{water}}(P)$.[49] In order to explore phase space, translation, rotation and swap moves were applied to water molecules, in a ratio of 1:1:2 respectively. Each simulation consists of $2\times\ 10^5$ equilibration cycles followed by 10^5 production cycles, during which average quantities were calculated.

In order to probe electrolyte insertion in zeosils in the osmotic ensemble, we used our recently released implementation version of the NCMC move[55] with a relative probability set to 10^{-3}. The NCMC move consists of $\mathcal{T} = 200$ steps, each one involving a perturbation of the system through interpolation of non-bonded parameters of the chosen molecules to be transformed, followed by relaxation with 200 MD steps with a timestep of 1 fs in the NVE ensemble. All simulations used a Nosé-Hoover thermostat, setting the temperature at 300 K. In addition, translations were performed both on ions and water while rotations were applied only to water molecules, in a ratio of 1:1:1 respectively. Each simulation was performed until 1000 values of the alchemical work had been gathered.

Then, we calculated the chemical potential $\Delta\mu_{C_nA_m}(P)$ in bulk electrolyte solutions containing 150 particles (composition given in Table S5), as in our previous study[55] but for pressure ranging from 0.006 to 1000 MPa. Because concentration depends explicitly on the volume of the solution, it is more convenient to use molality as the relevant metric.[54] This quantity will be required as input to set up the osmostat in zeosils filled with water molecules at different pressure. At each value of pressure, the simulation was performed until 400 values of the protocol work had been gathered to construct the $\Delta\mu_{C_nA_m}(P)$ relationship.

Finally, we also used the adapted NCMC move to calculate the chemical potential of water, as detailed in Ref. 55, and applied it to compute the chemical potential of water in electrolyte solutions $\mu^{C_nA_m}_{\text{water}}(P)$ of various molalities (Table S5) for pressure ranging from 0.006 to 1000 MPa. At each value of pressure, the simulation simulation was performed until 400 values of the protocol work had been gathered to construct the $\mu^{C_nA_m}_{\text{water}}(P)$ relationship.

Molecular Dynamics Simulations

Because of the sequential nature of the RASPA software, we used GROMACS[68] to perform MD simulations in the (N, P, T) ensemble to determine the density of systems with the same composition but four times bigger (600 particles) than those presented in Table S5. From these simulations, we extracted the average density and deduced the volume of the fixed

cubic box to perform MC simulations in RASPA and calculate $\Delta\mu_{C_nA_m}(P)$ and $\mu^{C_nA_m}_{\text{water}}(P)$ as explained above. The raw data presenting the relationship between applied pressure and density in electrolyte solution is given in Supporting Information.

Results and Discussion

Monte Carlo simulations of water intrusion/extrusion in zeosils

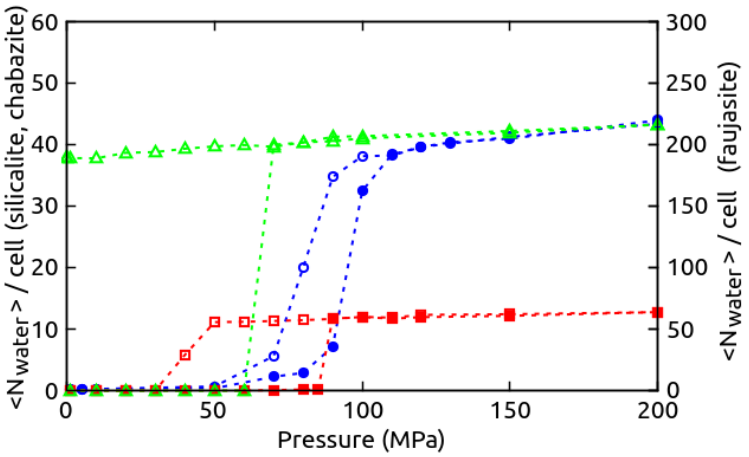

Figure 2: Water intrusion and extrusion isotherms computed through GCMC simulations at 300 K. Filled symbols refer to intrusion while open symbols refer to extrusion. Blue circles: silicalite-1; red squares: chabazite; green triangles: faujasite.

Figure 2 reports the adsorption and desorption isotherms of TIP4P water in silicalite-1, chabazite and faujasite zeosils. Given that the force field used for zeosils has been specifically designed to reproduce TIP4P water adsorption isotherm in silicalite-1 zeosil, we confirm the that adsorption isotherm calculated in this work for silicalite-1 is consistent with both previous GCMC simulations[49,63,69] and experiments,[9] as shown in Figure S1. Also, the intrusion pressure are similar for silicalite-1 and chabazite with values of respectively 95 MPa and 90 MPa while for the faujasite, it drops to 65 MPa. We do not expect a perfect agreement between the simulated and experimental intrusion isotherm of water in chabazite and faujasite, given that intrusion pressure is very sensitive to the choice of force field and other

structural features such as silanol defects. For instance, the experimental intrusion pressure of water in pure silica chabazite is about 32 MPa, lower than in our work[13]

Our results are in qualitative agreement with the Washburn equation,[70] as higher intrusion pressure is correlated with the smaller cage or channel diameter along our series of zeosils. Also, we analyzed the thermodynamics of water intrusion by calculating the adsorption heat q through the relationship:[71]

$$q = RT + \frac{\langle U^{\text{tot}} N \rangle - \langle U^{\text{tot}} \rangle \langle N \rangle}{\langle N^2 \rangle - \langle N \rangle^2} \tag{1}$$

where U^{tot} is the sum of host–guest and guest–guest interactions. In Figures S2 to S4, we report the evolution of the heat of intrusion and extrusion in each zeosil. The hydrophobic nature of the zeosils is clearly visible from the heat of adsorption at very low loading, which is dominated by interaction of water with the zeosil structure. In each case, the heat of adsorption is comprised between 20 and 30 kJ/mol, which is much lower that the bulk vaporization enthalpy of water (44 kJ/mol for TIP4P water at 300 K). After water intrusion, the heat of adsorption becomes higher than the bulk vaporization enthalpy of water, due to the formation of a dense liquid-like water phase in the pores of the zeosils. In this case, the heat of adsorption is dominated by interaction between water molecules.

Electrolyte intrusion in zeosils at different water loading

The process of water intrusion in zeosils is the initial step for further probing electrolyte intrusion in these materials. We use the final configuration of zeosil-water system at 200 MPa for chabazite and faujasite where 13.25 and 211 water molecules are adsorbed per cell, respectively, while for silicalite-1, the final system containing 53 water molecules per cell at 400 MPa is considered. We also investigate electrolyte intrusion at other water loadings. For proof-of-concept, we do not perform GCMC simulations for these cases but relax systems of zeosil-water at chosen loading by Monte Carlo simulation in the NVT ensemble for probing

the influence of water loading on the electrolyte intrusion. Consequently, we investigate loadings of 5, 10, 15, 20, 30 and 58.5 water molecules per cell in silicalite-1; for chabazite, systems characterized by 1.33, 2.66, 4, 5.33, 6.66, 8.33, 15 and 16.66 water molecules per unit cell are investigated. Finally, faujasite contains 20, 40, 80, 120, 215, 260 and 275 water molecules per unit cell.

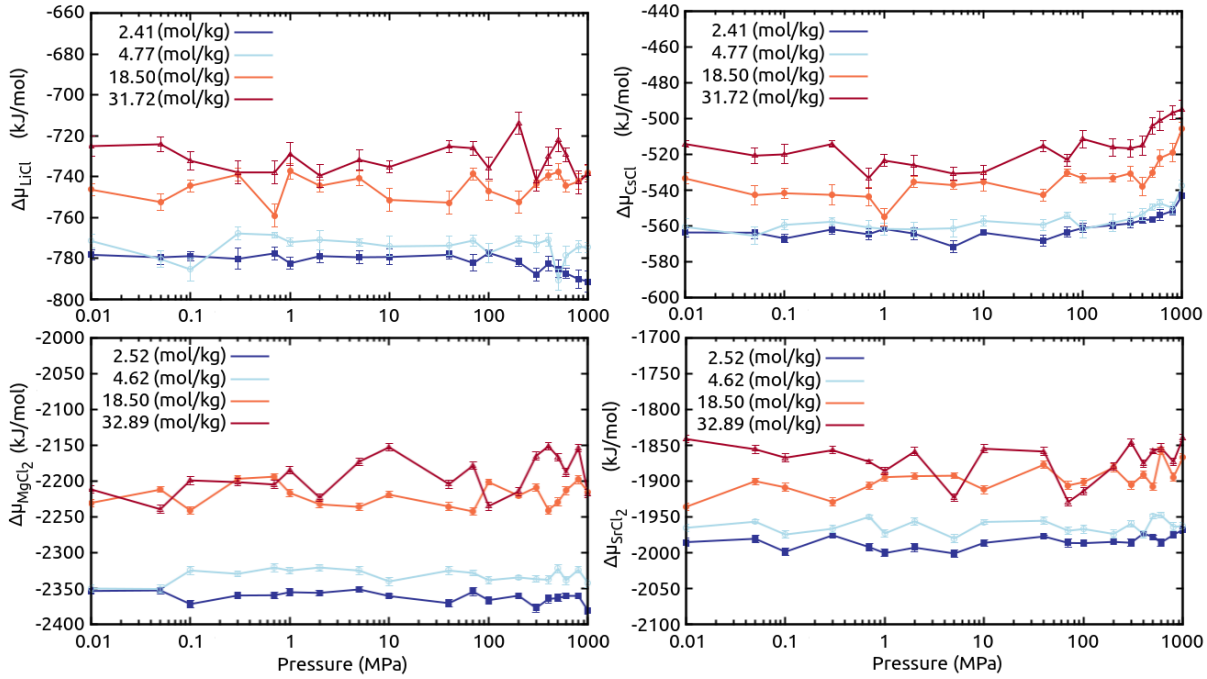

Figure 3: Chemical potential of ion exchange $\Delta\mu_{C_nA_m}(P)$ as a function of pressure. Top-left: evolution of $\Delta\mu_{\mathrm{LiCl}}(P)$. Top-right: evolution of $\Delta\mu_{\mathrm{CsCl}}(P)$. Bottom-left: evolution of $\Delta\mu_{\mathrm{MgCl_2}}(P)$. Bottom-right: evolution of $\Delta\mu_{\mathrm{SrCl_2}}(P)$.

It is required to calibrate the chemical potential $\Delta\mu_{C_nA_m}(P)$ as performed in our former work[55] for a wide range of pressure to assess electrolyte intrusion at 200 MPa in chabazite and faujasite and at 400 MPa in silicalite-1. These calculations are computationally expensive so that we investigated only two representative monovalent electrolytes which are LiCl and CsCl since Li^+ is the smallest cation (σ_{Li^+} = 1.505 Å) while Cs^+ is the largest one (σ_{Cs^+} = 3.883 Å) among the alkali-chloride electrolytes. For similar reason, we chose two divalent electrolytes which are $MgCl_2$ and $SrCl_2$. The evolution of $\Delta\mu_{C_nA_m}(P)$ is reported in Figure 3. For all cases, the chemical potential of ion exchange is fluctuating around a mean value over

the pressure investigated. It is understandable because no new particle are inserted in the system, only water molecules are replaced by ions. However, for CsCl, the chemical potential becomes more positive for pressure higher than 200 MPa. Consequently, we assume that chemical potential of ion exchange does not depend on the pressure up to 200 MPa, allowing us to use the chemical potential calculated in our former study[55] in this work.

The evolution of the alchemical work associated to the intrusion of an electrolyte unit in zeosils filled with water at 200 MPa (chabazite and faujasite) and 400 MPa (silicalite-1) is presented in Figure 4 while row values and error estimation can be found in Tables S6 and S7.

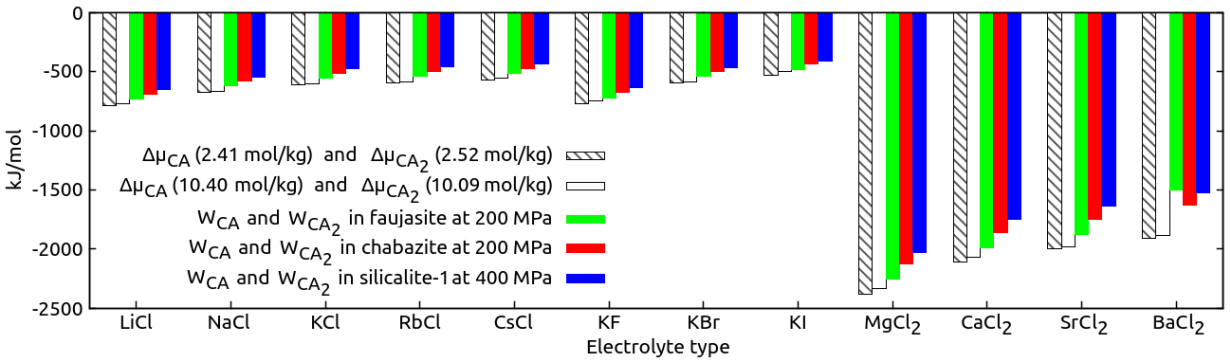

Figure 4: Histograms of the alchemical work W_{CA} for monovalent and W_{CA_2} for divalent-cation electrolytes associated to the intrusion of a single electrolyte unit in faujasite (green), chabazite (red) and silicalite-1 (blue). The chemical potential of ion exchange $\Delta\mu_{CA}$ for monovalent and $\Delta\mu_{CA_2}$ for divalent-cation electrolytes in the bulk for molalities of respectively 2.41, 10.40 and 2.52, 10.09 mol/kg are represented as dashed and white histograms.

The alchemical work is the lowest in the silicalite-1, and increases for chabazite and faujasite which is consistent with silicalite-1 channel diameter and chabazite and faujasite cage diameter. We deduce that a lower pore size is associated to a mediocre solvation of the ions, because the lack of available space does not allow water molecules to properly form solvation shells around the ions. The alchemical work is lower for every electrolytes investigated compared with $\Delta\mu_{C_nA_m}(P)$ for electrolyte bulk solution at different molalities but it is necessary to be more quantitative by calculating the associated probability for insertion of an electrolyte unit in the zeosils. We recall from our previous work[55] that the

probability for accepting an electrolyte unit is written as follows:

$$P_{acc} = \min\left(1, \frac{\prod_{i=0}^{m+n-1}\left(N_{H_2O}-i\right)}{\prod_{j=1}^{n}\left(N_{C^{m+}}+j\right)\prod_{k=1}^{m}\left(N_{A^{n-}}+k\right)} e^{-\beta\left(W_{C_nA_m}-\Delta\mu_{C_nA_m}\right)}\right) \tag{2}$$
$$= \min\left(1, N_{H_2O}\left(N_{H_2O}-1\right)e^{-\beta\left(W_{C_nA_m}-\Delta\mu_{C_nA_m}\right)}\right)$$

We estimate the probability of ion intrusion by using the raw values of the alchemical work and chemical potential reported in Tables S6 and S7. At bulk molality of 2.41 mol/kg for monovalent electrolytes CA the probability of ion intrusion is respectively about $\sim 10^{-6}$, $\sim 10^{-13}$ and $\sim 10^{-18}$-10^{-20} for faujasite, chabazite and silicalite-1. The probability of ion intrusion for divalent-cation electrolytes CA_2 at bulk molality of 2.52 mol/kg is lower than for monovalent electrolytes with probabilities of $\sim 10^{-18}$, $\sim 10^{-40}$ and $\sim 10^{-60}$ respectively, because it is less favorable to solvate simultaneously three ions in the zeosils than an ion pair in case of monovalent electrolytes. For bulk electrolyte at high molalities (i.e. at 10.40 mol/kg for monovalent electrolytes), the probability of electrolyte intrusion increases for all zeosils, but remains insignificant for silicalite ($\sim$$10^{-16}$-$10^{-17}$) and chabazite ($\sim$$10^{-10}$-$10^{-12}$). On the contrary, the probability of electrolyte intrusion in faujasite becomes significant ($\sim$$10^{-4}$-$\sim$$10^{-1}$), indicating that electrolyte may penetrate the zeosil at such concentration. Finally, in the presence of divalent electrolytes, insertion probability in the three zeosils also increases but remains low so that no electrolyte may be intruded as well. In Figure S8, we presented the distribution of the alchemical work for inserting a first NaCl unit in silicalite-1, chabazite and faujasite. The histogram queue for silicalite-1 and chabazite reveals that several intrusion of NaCl electrolyte are associated with insertion probabilities P_{acc} of $\sim 10^{-1}$ for bulk molality of 10.09 mol/kg. However, after eventual intrusion of a NaCl pair, it is unlikely that the pair remains in the framework because alchemical work associated with the reverse move for transforming the NaCl into water molecules (denoted as W_{-NaCl} in our former work[55]) is

the opposite of W_{NaCl} resulting in a very high probability ($P_{del} \propto e^{-\beta(\Delta\mu_{C_nA_m} - W_{C_nA_m})}$) to remove the ion pair.

In experiments, NaCl electrolyte at concentration of 2 M penetrates chabazite when only 7 water molecules per cell are adsorbed which is lower than loading of 14 water molecules obtained by GCMC simulations (Figure 2). Therein, we calculated the alchemical work required to solvate a single NaCl pair in zeosils at different water loadings. The results are reported in Figure S5 and reveal a lower alchemical work, associated with a worst solvation of the ions due to the low amount of water presents in the zeosils. On the contrary, at very high amount of water molecules the alchemical work also diminishes for faujasite and chabazite because the dense fluid in cages cannot accommodate easily the intruded ions. Our simulations does not catch electrolyte intrusion in chabazite as shown in experiments[21] which may be attributed to the absence of defects in our models of zeosil or even other phenomenon that are not taken into account using classical force field such as reactivity of water with zeolites. Nontheless, it was shown by in situ X-ray diffraction experiments on NaCl aqueous solutions intrusion in pure silica chabazite[21] and LTA-type zeosil[30] that only the water molecules penetrate firstly (or at low pressure) into the pores, and we will work henceforth within this hypothesis.

Chemical potential of water in electrolyte solutions

Assuming that only water molecules but no electrolytes penetrate the zeosils, it is required to probe the evolution of water chemical potential in electrolyte solutions $\mu_{\text{water}}^{C_nA_m}(P)$. In case of pure water, there are three ways to derive the $\mu_{\text{water}}(P)$ relationship. From mercury porosimetry experiments, Porcheron and Monson[72] integrated the Gibbs–Duhem equation while Chempath and co-workers[73] computed the chemical potential of the vapor with equilibrium to the liquid at a given temperature by using the Peng–Robinson equation of state. The third approach consists in using molecular simulation to calculate water chemical potential as performed by Desbiens *et al.*[49] for the rigid TIP4P water model. A set of (N,P,T)

simulations is performed in order to obtain the relationship between pressure and density. The chemical potential as a function of the density is subsequently calculated by using ($\mu_{\text{water}}(P)$,V,T) simulations so that the density is used as an intermediate quantity easy to compute in order to obtain the $\mu_{\text{water}}(P)$ relationship. In our work, another approach is proposed : we performed (N,P,T) MD simulations to retrieve the density that is used to fix the simulation box in RASPA to run subsequent (N,V,T) simulations where the NCMC move is used to compute $\mu_{\text{water}}(P)$ with our adapted version of the Widom insertion technique. The comparison between different methods to calculate $\mu_{\text{water}}(P)$ is reported on Figure 5.

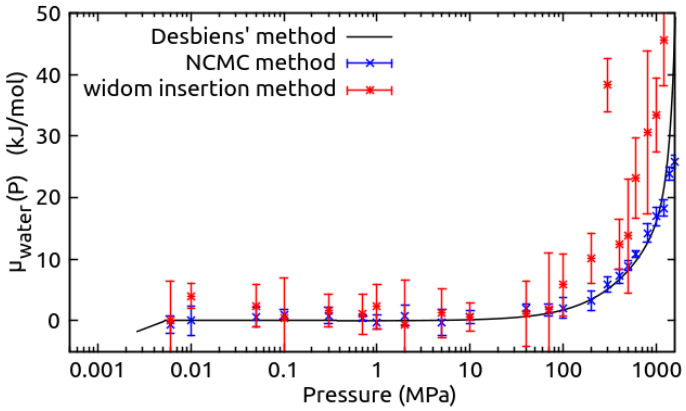

Figure 5: Chemical potential of TIP4P water estimated by three methods. Black curve : Desbiens' method. Blue points : Widom insertion method combined with NCMC move. Red points : Standard Widom insertion method.

For the sake of comparison, we run the same (N, V, T) simulation but use instead Widom insertion moves to estimate the $\mu_{\text{water}}(P)$ relationship. It is clear that this last approach is not suited for the computation of the chemical potential in such dense fluid because the probability of intrusion is very low due to an overestimation of the chemical potential at high pressure induced by interpenetration of sample molecule with other water molecules.[74] On the contrary, by using the NCMC move, the system is relaxed during insertion of the sample molecule and the chemical potential calculated with the modified Widom technique[55] is in agreement with those calculated by Desbiens and co-workers. In addition, we verify that both methods yields the same slope of chemical potential of pure water as a function of pressure (e.g., same molar volume $v_{\text{water}}(P)$), as shown in Figure S7.

Although the method proposed by Desbiens and co-workers is suitable for pure water, we did not apply it to determine the $\mu_{\text{water}}^{C_nA_m}(P)$ relationship for electrolyte solutions. Although there is no trouble in performing (N,P,T) simulation of electrolyte solutions to obtain the density as a function of pressure, the drawback comes from the ($\mu_{\text{water}}^{C_nA_m}(P)$,V,T) simulations where $\mu_{\text{water}}^{C_nA_m}(P)$ needs to be determined as a function of density. The chemical potential $\mu_{\text{water}}^{C_nA_m}(P)$ as input parameter dictates the evolution of the number of water molecules in the system except that the number of electrolyte units must also varies accordingly to keep a constant electrolyte concentration. In order to adress such issue, we used the NCMC move to compute $\mu_{\text{water}}^{C_nA_m}(P)$ as this method has been successfully applied to calculated $\mu_{\text{water}}(P)$ for pure TIP4P water. The results for LiCl, NaCl and CsCl electrolyte units at two different molalities are presented in Figure 6.

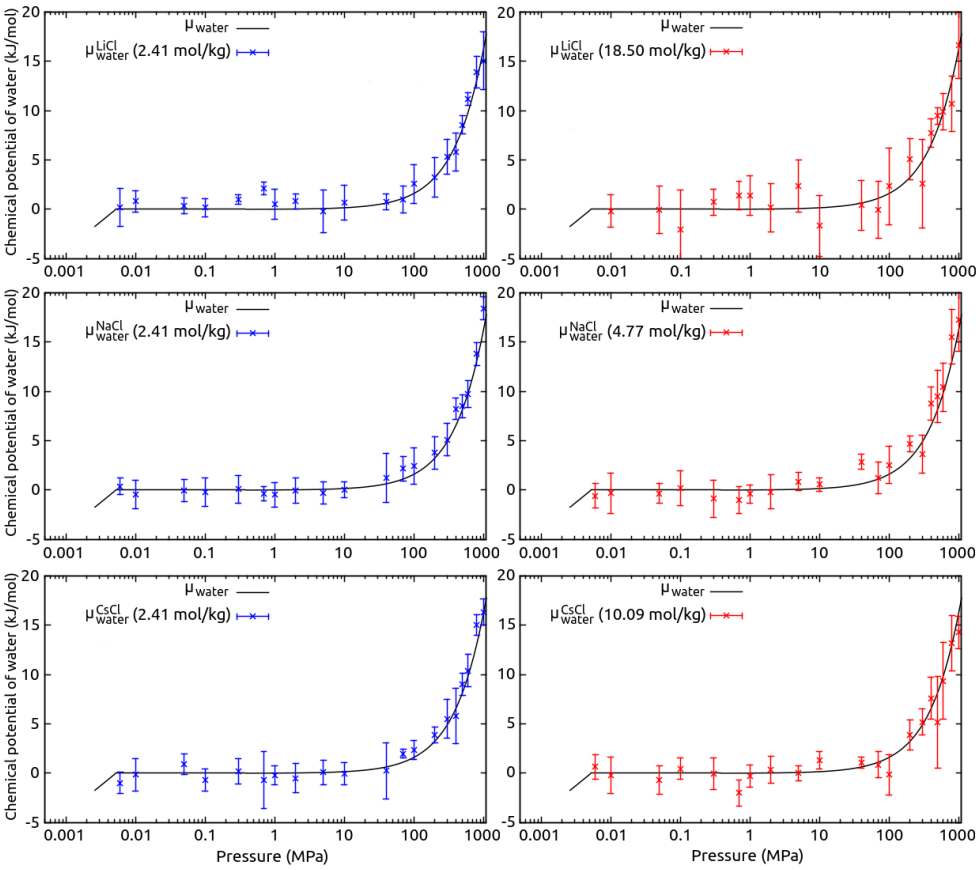

Figure 6: Chemical potential of TIP4P water in electrolyte solutions. Top: $\mu_{\text{water}}^{LiCl}(P)$; middle : $\mu_{\text{water}}^{NaCl}(P)$; bottom : $\mu_{\text{water}}^{CsCl}(P)$ at different molalities. The chemical potential of pure water is shown as black line in each plot for comparison.[49]

Here, the chemical potential of water in electrolyte solutions $\mu_{\text{water}}^{C_nA_m}(P)$ has been computed starting from 0.006 MPa, which is slightly higher than the vapor pressure of pure TIP4P water (0.0053 MPa) and vapor pressure of any electrolyte solution in this work. We do not focus on pressure below this value because the evolution of the vapor pressure of electrolyte solution in this range of pressure will be discussed later in the manuscript. The common trend is that the chemical potential of water in electrolyte solutions shows the same dependency in pressure as the chemical potentiel in pure water and this observation holds also for divalent-cation electrolytes ($\mu_{\text{water}}^{\text{MgCl}_2}(P)$ and $\mu_{\text{water}}^{\text{BaCl}_2}(P)$ as shown in Figure S10).

In order to further support our results, we calculate from experimental electrolyte densities $\rho_{\text{sol}}(P)$ and partial molar volume of electrolytes $v_{C_nA_m}(P)$[75] the molar volume of water $v_{\text{water}}^{C_nA_m}(P)$ in electrolyte solutions up to ∼40 MPa using the following relationship:

$$v_{\text{water}}^{C_nA_m}(P) = \frac{M_{\text{water}} - \rho_{\text{sol}}(P) x_{C_nA_m} \left(\frac{M_{\text{water}}}{M_{C_nA_m}}\right) v_{C_nA_m}(P)}{\rho_{\text{sol}}(P) x_{\text{water}}} \tag{3}$$

where M_{water} and $M_{C_nA_m}$ are respectively the molar mass of water and electrolyte and x_{water} and $x_{C_nA_m}$ are the mass fraction of water and electrolyte in solution. In Figures S6 and S7, we plot $v_{\text{water}}^{C_nA_m}(P)$ for monovalent (LiCl, NaCl, KCl) and divalent ($MgCl_2$, $CaCl_2$) electrolytes up to molalities of 5 mol/kg as well as partial molar volume of pure water extracted from NIST data. It is clear from experiment that the partial molar volume of water in electrolyte solutions is the same as the partial molar volume of pure water, irrespective of concentration and valency of electrolyte, which is in agreement with Figure 6.

In the following, we will assume that the chemical potential of water in the presence of electrolyte will have the same dependency in pressure as for pure water.

The law of osmotic pressure revisited

The main result obtained from the simulations in the osmotic ensemble is that no ions penetrate the zeosils, only water molecules. The non-penetration of ions is therefore used as

the main hypothesis for the revision of the law of osmotic pressure presented in this section, by taking account explicitly the nature and concentration of the electrolyte solution. We previously demonstrated that chemical potential of water in electrolyte solutions displays the same dependency in pressure as for pure water, but differ in their vapor pressure — that depends on the nature and concentration of the electrolyte.

Foremost, let us recall the link between chemical potential $\mu_{\text{water}}(P)$, fugacity f and fugacity coefficient ϕ for TIP4P water. In Figure S7, we present the chemical potential of pure TIP4P water $\mu_{\text{water}}(P)$ and the chemical potential of perfect gas $\mu_{gas}(P)$. The reference pressure is chosen to be the vapor pressure of water $P^{\text{vap}}_{\text{water}} = 5300$ Pa[49] for which chemical potential of water is set to zero. The chemical potential of perfect gas is written as follows:

$$\mu_{gas}(P) = \frac{1}{\beta} \ln \left(\frac{P}{P^{\text{vap}}_{\text{water}}} \right) \tag{4}$$

where $\beta = \frac{1}{k_B T}$. The acceptation probability of insertion and deletion of a water molecule in a given system can be written as a function of pressure:[76]

$$\begin{aligned} acc(N_{H_2O} \rightarrow N_{H_2O} + 1) &= \min \left(1, \frac{V \beta \phi P}{N_{H_2O} + 1} e^{-\beta (U_{N_{H_2O}+1} - U_{N_{H_2O}})} \right) \\ acc(N_{H_2O} \rightarrow N_{H_2O} - 1) &= \min \left(1, \frac{N_{H_2O}}{V \beta \phi P} e^{-\beta (U_{N_{H_2O}-1} - U_{N_{H_2O}})} \right) \end{aligned} \tag{5}$$

where V is the volume of the system and ϕ the fugacity coefficient at pressure P. The chemical potential is related to the pressure of the reservoir by $\mu_{\text{water}}(P)$ relationship, and it is more convenient to use pressure rather than chemical potential as input in a GCMC simulation, because chemical potential is defined from an arbitrary reference state. The fugacity coefficient ϕ appearing in Equation 5 is the Boltzmann factor of the difference in chemical potential between the gas phase and the liquid phase denoted by $\Delta\tilde{\mu}(P)$ in Figure S7 at a given pressure P:

$$\phi = e^{-\beta(\Delta\tilde{\mu}(P))} = e^{-\beta(\mu_{gas}(P) - \mu_{\text{water}}(P))} \tag{6}$$

which allows us to get rid of the reference state of the chemical potential because ϕ only depends on the relative difference of chemical potentials. Consequently, the chemical potential of liquid water is set to zero at the vapor pressure. The fugacity f appearing in Equation 5 is the product of the pressure and the fugacity coefficient:

$$f = \phi P \tag{7}$$

If the input pressure P in Equation 5 is below $P^{\text{vap}}_{\text{water}}$, water remains in its gaseous phase so that $\phi = 1$ and the pressure is indeed equal to fugacity. On the contrary, if the pressure is above $P^{\text{vap}}_{\text{water}}$, the fugacity coefficient drops ($\phi < 1$) and the fugacity is thus below to the real pressure P. The fugacity f is the pressure that the hypothetical perfect fluid would have for its chemical potential to be the same as the chemical potential of the real fluid at pressure P.[76]

Let us introduce the two following systems: the first one consists of a given zeosil in equilibrium with a reservoir of pure water while the second system deals with the same zeosil, but the reservoir is replaced with an electrolyte solution. Then, a certain intrusion pressure P_{water} is required, resulting in an intrusion of a certain amount of water inside the zeosil of the first system, in equilibrium with the reservoir of water. Since we hypothesize that only water molecules are intruded/extruded in the zeosils in the presence of electrolyte solutions, we want to determine the intrusion pressure $P^{C_nA_m}_{\text{water}}$ that must be applied to the zeosil of the second system surrounding by the electrolyte solution, to obtain the same amount of intruded water molecules at equilibrium as for the first system. In order to find exactly the same amount of water molecules in both zeosils, the probabilities in Equation 5 must be the same for the two systems. In other words, it requires the fugacity of pure water f_{water} and water in the electrolyte solution $f^{C_nA_m}_{\text{water}}$ to be equal:

$$f_{\text{water}} = f^{C_nA_m}_{\text{water}} \tag{8}$$

It has been shown that LiCl and NaCl electrolyte solutions have lower vapor pressure than pure water,[77] and assuming that chemical potential of water in electrolyte solutions has the same dependency in pressure as chemical potential of pure water, we plot respectively in Figure 7 the chemical potential of pure TIP4P water $\mu^{\text{pure}}_{\text{water}}(P)$ taken from Desbiens and co-workers for which $P^{\text{vap}}_{\text{water}}$ is equal to 5300 Pa and chemical potential of water in an electrolyte solution $\mu^{C_nA_m}_{\text{water}}(P)$ for which we choose a lower $P^{\text{vap}}_{C_nA_m}$ equals to 2300 as a proof-of-concept.

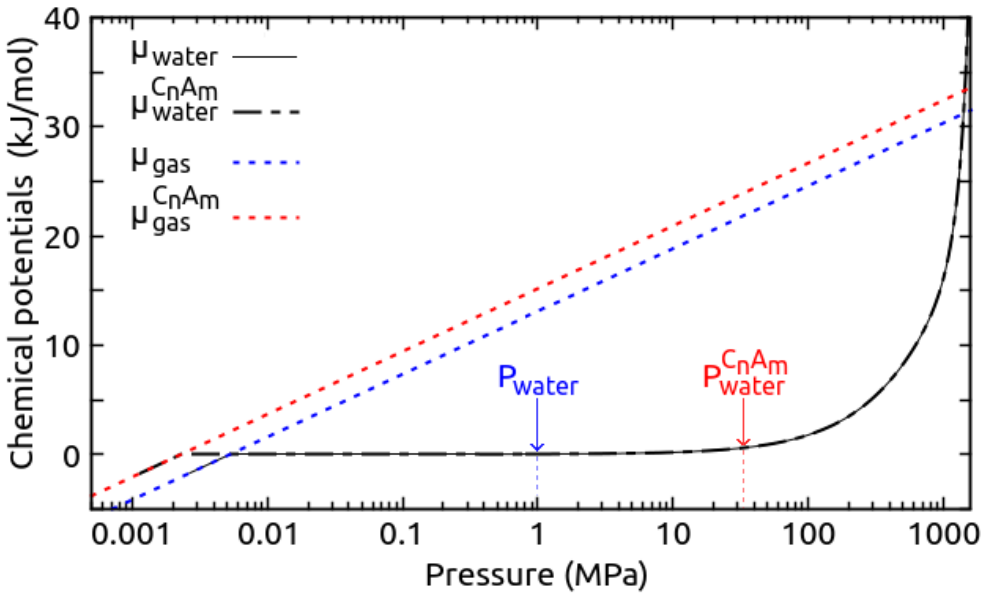

Figure 7: Chemical potential of pure water (full black curve) and water in electrolytes solution (dotted black curve), and respective curves of perfect gas in dotted blue and red lines. For instance, a hypothetical intrusion pressure P_{water} of 1 MPa (blue arrow) in a zeosil from a pure water reservoir corresponds to an intrusion pressure $P^{C_nA_m}_{\text{water}}$ of 33.5 MPa of water in the same zeosil, from the electrolyte solution reservoir, both characterized by the same acceptation probabilities of water intrusion (Equation 5).

Hence, the $\mu^{C_nA_m}_{\text{water}}(P)$ relationship is simply the $\mu_{\text{water}}(P)$ relationship extented to $P^{\text{vap}}_{C_nA_m}$ so that we have $\mu^{C_nA_m}_{\text{water}}(P^{\text{vap}}_{C_nA_m})$ equals also to zero. Consequently, although the fugacities are equals (Eqn. 8), the chemical potential of water in the electrolyte reservoir $\mu^{C_nA_m}_{\text{water}}(P)$ is thus different from the chemical potential of pure water reservoir $\mu_{\text{water}}(P)$. Let us rewrite Equation 8 in term of pressure and fugacity coefficient

$$\phi_{\text{water}} P_{\text{water}} = \phi^{C_nA_m}_{\text{water}} P^{C_nA_m}_{\text{water}} \tag{9}$$

We introduce the difference of chemical potential between the real fluid and perfect gas in both sides, leading to the following expression

$$e^{-\beta(\mu_{gas}(P_{\text{water}})-\mu_{\text{water}}(P_{\text{water}}))}P_{\text{water}} = e^{-\beta(\mu_{gas}^{C_nA_m}(P_{\text{water}}^{C_nA_m})-\mu_{\text{water}}^{C_nA_m}(P_{\text{water}}^{C_nA_m}))}P_{\text{water}}^{C_nA_m} \tag{10}$$

The chemical potential of gas phase for both water and water in the presence of electrolyte are written as:

$$\mu_{gas}(P) = \frac{1}{\beta}\ln\left(\frac{P}{P_{\text{water}}^{\text{vap}}}\right) \qquad \mu_{gas}^{C_nA_m}(P) = \frac{1}{\beta}\ln\left(\frac{P}{P_{C_nA_m}^{\text{vap}}}\right) \tag{11}$$

Then, inserting equations 11 in Equation 10 yields the following relationship

$$\mu_{\text{water}}(P_{\text{water}}) = \frac{1}{\beta}\ln\left(\frac{P_{C_nA_m}^{\text{vap}}}{P_{\text{water}}^{\text{vap}}}\right) + \mu_{\text{water}}^{C_nA_m}(P_{\text{water}}^{C_nA_m}) \tag{12}$$

Let us fit the chemical potentials $\mu_{\text{water}}(P_{\text{water}})$ and $\mu_{\text{water}}^{C_nA_m}(P_{\text{water}}^{C_nA_m})$ by a quadratic polynomial, to take into account of the increase of chemical potential and thus compression of water at high pressure:

$$\begin{aligned}\mu_{\text{water}}(P_{\text{water}}) &= AP_{\text{water}}^2 + BP_{\text{water}} + C \\ \mu_{\text{water}}^{C_nA_m}(P_{\text{water}}^{C_nA_m}) &= A\left(P_{\text{water}}^{C_nA_m}\right)^2 + BP_{\text{water}}^{C_nA_m} + D\end{aligned} \tag{13}$$

where A and B denote the same dependency of pressure for these chemical potentials, while C and D are differents because we have chosen $\mu_{\text{water}}(P_{\text{water}}^{\text{vap}})$ and $\mu_{\text{water}}^{C_nA_m}(P_{C_nA_m}^{\text{vap}})$ to be equal to zero. The polynomials 13 are introduced in Equation 12 in order to obtain a quadratic equation linking P_{water} and $P_{\text{water}}^{C_nA_m}$

$$A(P_{\text{water}}^{C_nA_m})^2 + BP_{\text{water}}^{C_nA_m} + \left(\frac{1}{\beta}\ln\left(\frac{P_{C_nA_m}^{\text{vap}}}{P_{\text{water}}^{\text{vap}}}\right) - AP_{\text{water}}^2 - BP_{\text{water}} + D - C\right) = 0 \tag{14}$$

The resolution of Equation 14 provides an analytical relationship between P_{water} and $P_{\text{water}}^{C_nA_m}$

$$P_{\text{water}}^{C_nA_m} = \frac{-B + \sqrt{\left(2AP_{\text{water}} + B\right)^2 - \frac{4A}{\beta}\ln\left(\frac{P_{C_nA_m}^{\text{vap}}}{P_{\text{water}}^{\text{vap}}}\right) + 4A(C-D)}}{2A} \tag{15}$$

The above fits of polynomials 13 leads to values of -1.44027×10^{-6} kJ·mol^{-1}·MPa^{-2}; 1.74119×10^{-2} kJ·mol^{-1}·MPa^{-1}; 2.47448×10^{-2} kJ·mol^{-1} and 2.47978×10^{-2} kJ·mol^{-1} for A,B,C and D coefficients. Consequently, the term $4A(C-D)$ is about $\sim 10^{-10}$ MPa^2, which is much lower than the other terms in the equation and thus can be ignored. This assumption is valid for any electrolyte solution in our model because it would have a vapor pressure lower than vapor pressure of pure water. Also, the chemical potential profile is very flat at low pressure resulting in very close values of the constant coefficient of the quadratic fit for chemical potential of pure water C and for water in electrolyte solutions D. Therein, Equation 15 becomes

$$P_{\text{water}}^{C_nA_m} \approx \frac{-B + \sqrt{\left(2AP_{\text{water}} + B\right)^2 - \frac{4A}{\beta}\ln\left(a_{\text{water}}^{C_nA_m}\right)}}{2A} \tag{16}$$

where we introduced the activity of water in the electrolyte solution $a_{\text{water}}^{C_nA_m}$ being the ratio between $P_{C_nA_m}^{\text{vap}}$ and $P_{\text{water}}^{\text{vap}}$. Equation 16 is the analytical model used subsequently to predict the intrusion pressure of electrolyte solution in zeosils. In Figure 7, we select an hypothetical intrusion pressure P_{water} of 1 MPa from the pure water reservoir and deduce using Equation 16 that the corresponding intrusion pressure of water from the electrolyte solution reservoir leading to the same acceptation probabilities of water intrusion (Eqn. 5) is 33.5 MPa. This example shows qualitatively that a decrease of vapor pressure of a solution due to presence of electrolyte is consistent with a shift of intrusion pressure towards higher values. Our model requires as input the water activity in electrolyte solutions $a_{\text{water}}^{C_nA_m}$ over a wide range of concentration in order to rationalize intrusion pressure of electrolyte solutions

in zeosils. There has been a large effort in order to obtain thermodynamic data (osmotic coefficient, activity coefficients...) of electrolyte solutions, either acquired experimentally to build theoretical models or through molecular simulations. The most widespread computational technique is the Gibbs Ensemble Monte Carlo method[76,78–80] based on particle exchange between two reservoirs containing the two phases in equilibrium (e.g. liquid and vapor phase for water). Unfortunately, Gibbs Ensemble Monte Carlo method in combination with the atomistic force field as used in our study make these simulations costly to predict precisely vapor pressure of electrolyte solutions. Another approach is the grand canonical screening technique[77,81] used to determine the point of liquid-vapor coexistence for systems in contact with vacuum. The vapor pressure of LiCl and NaCl has been obtained from screening various chemical potential using GCMC simulations, but using a coarse-grained description of electrolyte solutions. Consequently, this approach has the same limitation as for the Gibbs Ensemble Monte Carlo method to be used in combination with atomistic force fields. Also, another straightforward approach used a modified Widom insertion Method[82] to compute the activity coefficient of electrolyte, but in implicit water solvation making it unsuitable for atomistic force field either. Theoretical models based on experimental thermodynamic data are alternative approaches to predict vapor pressure (and by extension activity of water) in electrolyte solutions. The Debye–Hückel theory provides analytical equations to calculate activity and osmostic coefficients, but its validity domains is about of $\sim$0.01 M because of the neglect of short range interactions, ion size and ion-ion correlations.[83] There has been a huge effort devoted to extend the applicability range of the Debye–Hückel theory by adding the above effects through fitting parameters. Along this line, the specific interaction theory[84–86] uses experimental equilibrium constant at different ionic strength to determine activity coefficients for a wide range of concentration. A more sophisticated model has been proposed by Pitzer[87] by which activity and osmotic coefficients of single as well as mixed electrolytes at different temperatures can be modeled up to molalities of $\sim$ 10 mol/Kg, at the expense of a higher number of fitting parameters. We decided to use the Pitzer model in our work,

not only because it is a sophisticated model that has been widely used in the literature but it has has been extented for various electrolyte combinations and concentrations.[88–91] The version 0.5.2 of the Pytzer simulation package[92] is the state of the art summarizing the pitzer parameters available in the literature for the series of electrolytes used in this work. We calculated with the Pytzer package the activity of water $a_{\text{water}}^{C_nA_m}$ (Figure 8) as well as the mean activity coefficient of electrolytes $\gamma_{C_nA_m}$ (Figures S8 to S10) up to saturation molality for each electrolyte of our study (Table S8). We also provide raw data for all electrolytes in Tables S9 to S20.

First, at low electrolyte molality for all cases the activity of water obeys the Raoult's law. There is a clear correlation between a decrease of ion radius and deviation from the Raoult's law at high molality as shown by the drop of water activity for LiCl and KF electrolytes (top and middle panel of Figure 8). This is attributed to the higher solvation of water in the presence of smaller ions[55] that contributes to lower activity of water and conversely increases activity coefficient of electrolytes $\gamma_{C_nA_m}$ (Figures S8 to S10). Also, the effect of cation charge is cleary visible for divalent-cation electrolyte as water activity for all cases drops at low molality compared to monovalent electrolytes (bottom panel, Figure 8). Finally, the Pitzer model reproduces the experimental activity coefficient of electrolytes $\gamma_{C_nA_m}$ except up to 10 mol/kg for LiCl, so that we can use the values of $a_{\text{water}}^{C_nA_m}$ to predict intrusion pressure for electrolyte solutions in zeosils, knowing the intrusion pressure in pure water by using Equation 16.

Prediction of intrusion/extrusion pressure in porous materials

We introduced the above analytical model in the context of zeosils, but it can be applied to various hydrophobic porous materials such as MOFs, provided that the same hypotheses are satisfied (i.e. no alteration of the porous material and only water molecules intruded inside it). We compare experimental data for intrusion pressure of various zeosils[58] with prediction obtained from our analytical model and with the van 't Hoff law of osmotic pressure expressed

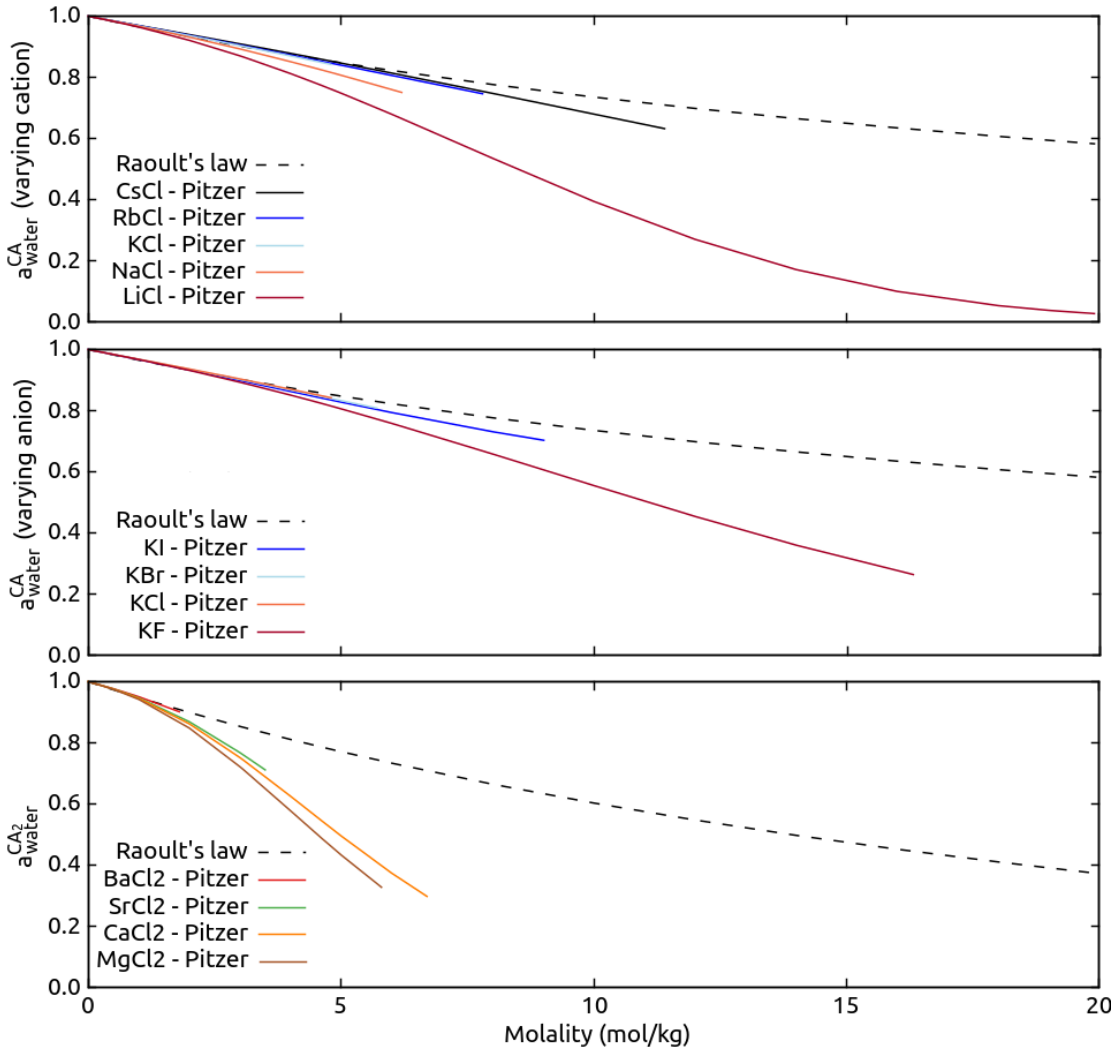

Figure 8: Activity of water in electrolyte solutions $a^{C_nA_m}_{\text{water}}$ up to saturation molality. Top: alkali-chloride electrolyte solutions; middle: potassium-halide electrolyte solutions; bottom: earth alkali-chloride electrolyte solutions. The dotted line indicates activity coefficient obtained from the Raoult's law.

as follows:

$$P_{\text{water}}^{C_nA_m} = P_{\text{water}} + imRT \tag{17}$$

where i is the number of ions per electrolyte unit, R is the ideal gas constant, T is the temperature and m the molality in mol/kg. For monovalent electrolytes, we have $i = 2$ and $iRT = 4.99$ MPa·kg·mol^{-1} while for divalent-cation electrolytes, we have $i = 3$ and $iRT = 7.48$ MPa·kg·mol^{-1}.

We screen intrusion pressure of different electrolyte solutions in three zeosils which are silicalite-1, chabazite and *BEA-type zeosil. Figure 9 reports both experimental data[58] and prediction from our model, for a molality of 4.62 mol/kg, corresponding to a ratio of 12 water molecules per electrolyte unit C_nA_m. Our model reproduces experimental intrusion pressures except for KF where the experimental intrusion is much lower than predicted. This could be attributed to the formation of silanol defects upon reaction of SiO_2 of HF acid appearing from hydrolysis of water due to F^- anions.

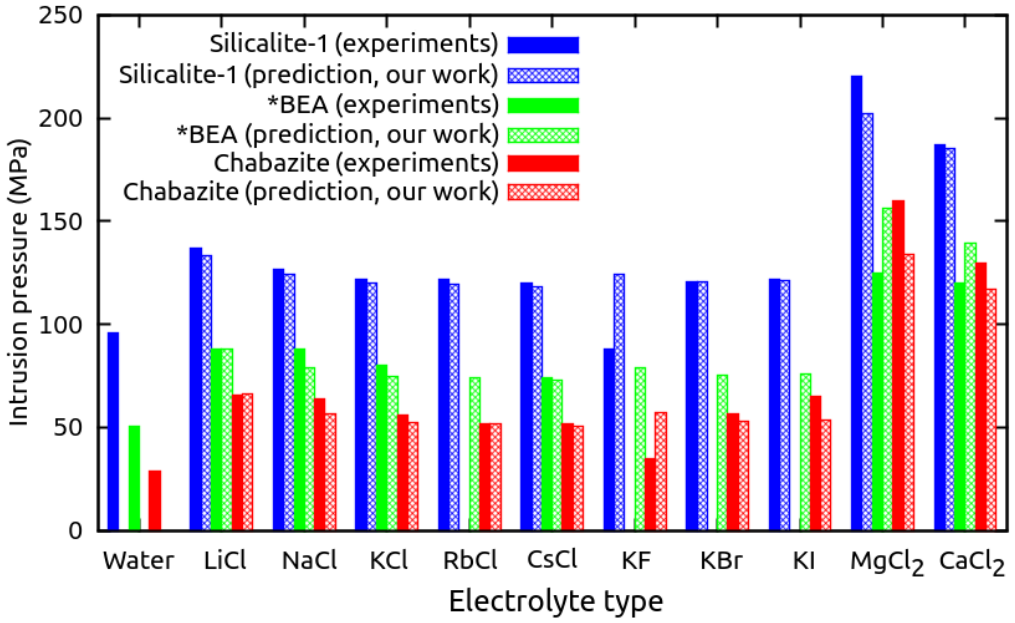

Figure 9: Intrusion pressure of water and electrolyte solutions (molality of 4.6 mol/kg) in silicalite-1 (blue), chabazite (red) and *BEA-type zeosil (green). Full histograms : experimental intrusion pressures;[58] dashed histograms : predicted intrusion pressure with Equation 16.

In Figure S11, we provide in addition the histogram of intrusion pressures predicted by the van 't Hoff law of osmotic pressure that both underestimates for most electrolytes the intrusion pressure and does not distinguish between electrolytes that produce the same ideal entropy of mixing, because at the studied concentration, electrolytes are non ideal as previously shown in Figure 8. The small variation of intrusion pressure existing within the series of electrolytes that can be rationalized in term of activity of water depends on the concentration and of the nature of the electrolyte, providing that input activity coefficients are properly parameterized. It is crucial from a practical point of view because at a given concentration, the electrolyte solution characterized by the lowest water activity such as LiCl results in the highest intrusion pressure and thus stored energy inside the material. This latter point is not taken into account by the van 't Hoff law for which electrolytes behave as ideal solutions.

Conclusions

We have investigated electrolyte intrusion for various electrolyte solutions using molecular simulation and a revisited version of the law of osmotic pressure. We performed simulations on three representative pure-silica zeolites that are silicalite-1 (MFI type), chabazite (CHA type) and faujasite (FAU type) that were chosen to highlight the nature of the intruded fluid along their increasing pore diameter.

Before probing electrolyte intrusion, we reproduced by GCMC simulations the isotherm of water intrusion and extrusion for pure water in these zeosils and demonstrate that we reproduce intrusion pressures consistent with the literature. Then, we used the equilibrated zeosils with the water reservoir at high pressure as the initial state to perform Monte Carlo simulations in the osmotic ensemble using our version of the NCMC move. The alchemical work (i.e. the work performed by the system) for inserting a single electrolyte unit is associated to a very low probability of intrusion in silicalite-1 and chabazite while for faujasite,

there could be intrusion of electrolyte because of the larger pore allowing a better solvation of the ions. The non-intrusion of electrolytes in the low pore diameter zeosils are consistent with experiments reporting only water as the first intruded species in chabazite and LTA-type zeosils.

Assuming that only water molecules penetrate in low-pore diameter zeosils, we determined how the chemical potential of water evolves in the presence of electrolytes. By performing a series of Monte Carlo simulations using our adapted NCMC move, we showed that chemical potential of water in electrolyte solutions displays the same dependency in pressure as chemical potential of pure water.

Finally, we revisit the law of osmotic pressure by proposing an analytical model for predicting water intrusion in zeosils. The shift of intrusion pressure towards greater values is directly induced by a drop of the activity of water and thus by a decrease of the vapor pressure of electrolyte solutions. The van 't Hoff law is not suited to calculate pressure beyond concentration of $\sim$2 M because activity coefficient of water deviates from Raoult's law and depends clearly of the nature of the electrolyte of interest. Instead, we use the Pitzer model to calculate activity of water for various electrolyte solutions up to saturation concentration. Our model was able to reproduce experimental intrusion pressure in various zeosils (silicalite-1, chabazite en *BEA-type zeosil) for different electrolytes at relatively high concentration (molality of $\sim$4.62 mol/kg), showing that our model accounts of both concentration and nature of the electrolyte solution. On the contrary, the van 't Hoff law of osmotic pressure assumes electrolyte solutions to be ideal and does not reproduce not only the small variation of intrusion pressure existing in the presence of monovalent electrolytes but clearly understimates intrusion pressure for divalent-cation electrolytes. Hence, our model suggests that a high performance electrolyte for energy storage in nanoporous materials should have a low water activity to guarantee the highest intrusion pressure. We note, however, that the presence of silanol defects in zeosils increases their hydrophilicity and therefore decreases the intrusion pressure. In order to decipher the role of the silanol defects from the pore diameter

on the intrusion pressure and the nature of the intruded fluid, we intend in the future to extend our methodology to more realistic zeosil models including silanol defects.

Acknowledgement

This work was funded by Agence Nationale de la Recherche under project MESAMM (ANR-19-CE05-0031). Access to high-performance computing platforms was provided by GENCI grant A0150807069.

Supporting Information Available

Force field parameters, heat of adsorption of water in zeosils, raw data and supplemental data for alchemical work, chemical potentials, as well as activity coefficients.

References

(1) Eroshenko, V. Heterogeneous structure for accumulation or dissipation of energy, process to use it and associated devices. *Pat. WO* **1996**, *96*, 18040.

(2) Eroshenko, V. Eroshenko hydrocapillary accumulator. *URSS patent* **1985**, *1333870*, 24.

(3) Eroshenko, V.; Popyk, A. Current Status and Perspectives of Thermomolecular Engine Developments. *Int. J. Thermodyn.* **2014**, *17*.

(4) Coiffard, L.; Eroshenko, V. A.; Grolier, J.-P. E. Thermomechanics of the variation of interfaces in heterogeneous lyophobic systems. *AIChE journal* **2005**, *51*, 1246–1257.

(5) Laouir, A.; Luo, L.; Tondeur, D.; Cachot, T.; Le Goff, P. Thermal machines based on surface energy of wetting: Thermodynamic analysis. *AIChE Journal* **2003**, *49*, 764–781.

(6) Eroshenko, V.; Piatiletov, I.; Coiffard, L.; Stoudenets, V. A new paradigm of mechanical energy dissipation. Part 2: Experimental investigation and effectiveness of a novel car damper. *Proceedings of the Institution of Mechanical Engineers, Part D: Journal of Automobile Engineering* **2007**, *221*, 301–312.

(7) Eroshenko, V. A new paradigm of mechanical energy dissipation. Part 1: theoretical aspects and practical solutions. *Proceedings of the Institution of Mechanical Engineers, Part D: Journal of Automobile Engineering* **2007**, *221*, 285–300.

(8) Suciu, C. V.; Iwatsubo, T.; Yaguchi, K.; Ikenaga, M. Novel and global approach of the complex and interconnected phenomena related to the contact line movement past a solid surface from hydrophobized silica gel. *J. Colloid Interface Sci.* **2005**, *283*, 196–214.

(9) Eroshenko, V.; Regis, R.-C.; Soulard, M.; Patarin, J. Energetics: a new field of applications for hydrophobic zeolites. *J. Am. Chem. Soc.* **2001**, *123*, 8129–8130.

(10) Trzpit, M.; Soulard, M.; Patarin, J. The pure silica Chabazite: A high volume molecular spring at low pressure for energy storage. *Chem. Lett.* **2007**, *36*, 980–981.

(11) Trzpit, M.; Soulard, M.; Patarin, J.; Desbiens, N.; Cailliez, F.; Boutin, A.; Demachy, I.; Fuchs, A. The effect of local defects on water adsorption in silicalite-1 zeolite: A joint experimental and molecular simulation study. *Langmuir* **2007**, *23*, 10131–10139.

(12) Cailliez, F.; Trzpit, M.; Soulard, M.; Demachy, I.; Boutin, A.; Patarin, J.; Fuchs, A. H. Thermodynamics of water intrusion in nanoporous hydrophobic solids. *Phys. Chem. Chem. Phys.* **2008**, *10*, 4817–4826.

(13) Trzpit, M.; Rigolet, S.; Paillaud, J.-L.; Marichal, C.; Soulard, M.; Patarin, J. Pure Silica Chabazite Molecular Spring: A Structural Study on Water Intrusion- Extrusion Processes. *J. Phys. Chem. B* **2008**, *112*, 7257–7266.

(14) Saada, M. A.; Rigolet, S.; Paillaud, J.-L.; Bats, N.; Soulard, M.; Patarin, J. Investigation of the energetic performance of pure silica ITQ-4 (IFR) zeolite under high pressure water intrusion. *J. Phys. Chem. C* **2010**, *114*, 11650–11658.

(15) Saada, M. A.; Soulard, M.; Marler, B.; Gies, H.; Patarin, J. High-pressure water intrusion investigation of pure silica RUB-41 and S-SOD zeolite materials. *J. Phys. Chem. C* **2011**, *115*, 425–430.

(16) Tzanis, L.; Trzpit, M.; Soulard, M.; Patarin, J. High pressure water intrusion investigation of pure silica 1D channel AFI, MTW and TON-type zeolites. *Microporous Mesoporous Mater.* **2011**, *146*, 119–126.

(17) Tzanis, L.; Trzpit, M.; Soulard, M.; Patarin, J. Energetic performances of channel and cage-type zeosils. *J. Phys. Chem. C* **2012**, *116*, 20389–20395.

(18) Tzanis, L.; Marler, B.; Gies, H.; Patarin, J. High-pressure water intrusion investigation of pure silica ITQ-7 zeolite. *J. Phys. Chem. C* **2013**, *117*, 4098–4103.

(19) Khay, I.; Tzanis, L.; Daou, T. J.; Nouali, H.; Ryzhikov, A.; Patarin, J. Energetic behavior of the pure silica ITQ-12 (ITW) zeolite under high pressure water intrusion. *Phys. Chem. Chem. Phys.* **2013**, *15*, 20320–20325.

(20) Tzanis, L.; Nouali, H.; Daou, T. J.; Soulard, M.; Patarin, J. Influence of the aqueous medium on the energetic performances of silicalite-1. *Mater. Lett.* **2014**, *115*, 229–232.

(21) Confalonieri, G.; Ryzhikov, A.; Arletti, R.; Nouali, H.; Quartieri, S.; Daou, T. J.; Patarin, J. Intrusion–extrusion of electrolyte aqueous solutions in pure silica chabazite by in situ high pressure synchrotron x-ray powder diffraction. *J. Phys. Chem. C* **2018**, *122*, 28001–28012.

(22) Arletti, R.; Ronchi, L.; Quartieri, S.; Vezzalini, G.; Ryzhikov, A.; Nouali, H.; Daou, T. J.; Patarin, J. Intrusion-extrusion experiments of MgCl2 aqueous solution

in pure silica ferrierite: Evidence of the nature of intruded liquid by in situ high pressure synchrotron X-ray powder diffraction. *Microporous Mesoporous Mater.* **2016**, *235*, 253–260.

(23) Ryzhikov, A.; Nouali, H.; Daou, T.; Patarin, J. A drastic influence of the anion nature and concentration on high pressure intrusion–extrusion of electrolyte solutions in Silicalite-1. *Phys. Chem. Chem. Phys.* **2018**, *20*, 6462–6468.

(24) Khay, I.; Daou, T.; Nouali, H.; Ryzhikov, A.; Rigolet, S.; Patarin, J. High pressure intrusion–extrusion of LiCl aqueous solutions in silicalite-1 zeolite: influence on energetic performances. *J. Phys. Chem. C* **2014**, *118*, 3935–3941.

(25) Ryzhikov, A.; Khay, I.; Nouali, H.; Daou, T.; Patarin, J. Drastic change of the intrusion–extrusion behavior of electrolyte solutions in pure silica* BEA-type zeolite. *Phys. Chem. Chem. Phys.* **2014**, *16*, 17893–17899.

(26) Kirschhock, C. E.; De Prins, M.; Verheijen, E.; Ryzhikov, A.; Daou, T. J.; Nouali, H.; Taulelle, F.; Martens, J. A.; Patarin, J. Intrusion–extrusion spring performance of–COK-14 zeolite enhanced by structural changes. *Phys. Chem. Chem. Phys.* **2016**, *18*, 18795–18801.

(27) Ronchi, L.; Ryzhikov, A.; Nouali, H.; Daou, T. J.; Patarin, J. Energetic performances of FER-type zeolite in the presence of electrolyte solutions under high pressure. *Energy* **2017**, *130*, 29–37.

(28) Kabalan, I.; Khay, I.; Nouali, H.; Ryzhikov, A.; Lebeau, B.; Albrecht, S.; Rigolet, S.; Fadlallah, M.-B.; Toufaily, J.; Hamieh, T. et al. Influence of the particle sizes on the energetic performances of MFI-type zeolites. *J. Phys. Chem. C* **2015**, *119*, 18074–18083.

(29) Ronchi, L.; Ryzhikov, A.; Nouali, H.; Daou, T. J.; Patarin, J. Energetic performances of pure-silica DDR zeolite by high-pressure intrusion–extrusion of electrolyte aqueous

solutions: A shock-absorber with huge absorbed energy. *J. Phys. Chem. C* **2018**, *122*, 2726–2733.

(30) Confalonieri, G.; Ryzhikov, A.; Arletti, R.; Quartieri, S.; Vezzalini, G.; Isaac, C.; Paillaud, J.-L.; Nouali, H.; Daou, T. J. Structural interpretation of the energetic performances of a pure silica LTA-type zeolite. *Phys. Chem. Chem. Phys.* **2020**, *22*, 5178–5187.

(31) Ryzhikov, A.; Ronchi, L.; Nouali, H.; Daou, T. J.; Paillaud, J.-L.; Patarin, J. High-pressure intrusion–extrusion of water and electrolyte solutions in pure-silica LTA zeolite. *J. Phys. Chem. C* **2015**, *119*, 28319–28325.

(32) Huve, J.; Daou, T. J.; Nouali, H.; Patarin, J.; Ryzhikov, A. The effect of nanostructures on high pressure intrusion–extrusion of water and electrolyte solutions in hierarchical nanoboxes of silicalite-1. *New J. Chem.* **2020**, *44*, 273–281.

(33) Ronchi, L.; Ryzhikov, A.; Nouali, H.; Daou, T.; Patarin, J. Influence of LiCl aqueous solution concentration on the energetic performances of pure silica chabazite. *New J. Chem.* **2017**, *41*, 2586–2592.

(34) Isaac, C.; Confalonieri, G.; Nouali, H.; Paillaud, J.-L.; Arletti, R.; Daou, T. J.; Ryzhikov, A. Unusual high-pressure intrusion-extrusion behavior of electrolyte solutions in Mu-26, a pure silica zeolite of topology STF. *Microporous Mesoporous Mater.* **2020**, *298*, 110047.

(35) Ronchi, L.; Nouali, H.; Daou, T. J.; Patarin, J.; Ryzhikov, A. Heterogeneous lyophobic systems based on pure silica ITH-type zeolites: High pressure intrusion of water and electrolyte solutions. *New J. Chem.* **2017**, *41*, 15087–15093.

(36) Confalonieri, G.; Daou, T. J.; Nouali, H.; Arletti, R.; Ryzhikov, A. Energetic performance of pure silica zeolites under high-pressure intrusion of LiCl aqueous solutions: an overview. *Molecules* **2020**, *25*, 2145.

(37) Ronchi, L.; Ryzhikov, A.; Nouali, H.; Daou, T. J.; Albrecht, S.; Patarin, J. Investigation of the energetic performance of pure silica BEC-type zeolite under high pressure water and 20 M LiCl intrusion-extrusion experiments. *Microporous Mesoporous Mater.* **2017**, *254*, 153–159.

(38) Ortiz, G.; Nouali, H.; Marichal, C.; Chaplais, G.; Patarin, J. Energetic performances of the metal–organic framework ZIF-8 obtained using high pressure water intrusion–extrusion experiments. *Phys. Chem. Chem. Phys.* **2013**, *15*, 4888–4891.

(39) Ortiz, G.; Nouali, H.; Marichal, C.; Chaplais, G.; Patarin, J. Versatile energetic behavior of ZIF-8 upon high pressure intrusion–extrusion of aqueous electrolyte solutions. *J. Phys. Chem. C* **2014**, *118*, 7321–7328.

(40) Fraux, G.; Coudert, F.-X.; Boutin, A.; Fuchs, A. H. Forced intrusion of water and aqueous solutions in microporous materials: from fundamental thermodynamics to energy storage devices. *Chem. Soc. Rev.* **2017**, *46*, 7421–7437.

(41) Michelin-Jamois, M.; Picard, C.; Vigier, G.; Charlaix, E. Giant osmotic pressure in the forced wetting of hydrophobic nanopores. *Phys. Rev. Lett.* **2015**, *115*, 036101.

(42) Ortiz, G.; Nouali, H.; Marichal, C.; Chaplais, G.; Patarin, J. Energetic performances of "ZIF-71–Aqueous solution" systems: a perfect shock-absorber with water. *J. Phys. Chem. C* **2014**, *118*, 21316–21322.

(43) Grosu, Y.; Eroshenko, V.; Nedelec, J. M.; Grolier, J. P. E. A new working mode for molecular springs: water intrusion induced by cooling and associated isobaric heat capacity change of a {ZIF-8 + water} system. *Phys. Chem. Chem. Phys.* **2015**, *17*, 1572–1574.

(44) Khay, I.; Chaplais, G.; Nouali, H.; Ortiz, G.; Marichal, C.; Patarin, J. Assessment of the energetic performances of various ZIFs with SOD or RHO topology using high pressure water intrusion–extrusion experiments. *Dalton Trans.* **2016**, *45*, 4392–4400.

(45) Mortada, B.; Chaplais, G.; Veremeienko, V.; Nouali, H.; Marichal, C.; Patarin, J. Energetic Performances of ZIF-8 Derivatives: Impact of the Substitution (Me, Cl, or Br) on Imidazolate Linker. *J. Phys. Chem. C* **2018**, *122*, 3846–3855.

(46) Sun, Y.; Li, Y.; Tan, J.-C. Framework flexibility of ZIF-8 under liquid intrusion: discovering time-dependent mechanical response and structural relaxation. *Phys. Chem. Chem. Phys.* **2018**, *20*, 10108–10113.

(47) Sun, Y.; Rogge, S. M. J.; Lamaire, A.; Vandenbrande, S.; Wieme, J.; Siviour, C. R.; Van Speybroeck, V.; Tan, J.-C. High-rate nanofluidic energy absorption in porous zeolitic frameworks. *Nat. Mater.* **2021**, *20*, 1015–1023.

(48) Mortada, B.; Chaplais, G.; Nouali, H.; Marichal, C.; Patarin, J. Phase transformations of metal–organic frameworks MAF-6 and ZIF-71 during intrusion–extrusion experiments. *J. Phys. Chem. C* **2019**, *123*, 4319–4328.

(49) Desbiens, N.; Boutin, A.; Demachy, I. Water condensation in hydrophobic silicalite-1 zeolite: a molecular simulation study. *The Journal of Physical Chemistry B* **2005**, *109*, 24071–24076.

(50) Ortiz, A. U.; Freitas, A. P.; Boutin, A.; Fuchs, A. H.; Coudert, F.-X. What makes zeolitic imidazolate frameworks hydrophobic or hydrophilic? The impact of geometry and functionalization on water adsorption. *Phys. Chem. Chem. Phys.* **2014**, *16*, 9940–9949.

(51) Han, A.; Lu, W.; Kim, T.; Chen, X.; Qiao, Y. Influence of anions on liquid infiltration and defiltration in a zeolite Y. *Phys. Rev. E* **2008**, *78*, 031408.

(52) Han, A.; Lu, W.; Kim, T.; Punyamurtula, V. K.; Qiao, Y. The dependence of infiltration pressure and volume in zeolite Y on potassium chloride concentration. *Smart materials and structures* **2009**, *18*, 024005.

(53) Washburn, E. W. Note on a method of determining the distribution of pore sizes in a porous material. *Proc. Nat. Acad. Sci.* **1921**, *7*, 115–116.

(54) Zamfir, S.; Moucka, F.; Bratko, D. High-Pressure Infiltration–Expulsion of Aqueous NaCl in Planar Hydrophobic Nanopores. *J. Phys. Chem. C* **2020**, *124*, 23433–23445.

(55) Izarra, A. d.; Coudert, F.-X.; Fuchs, A. H.; Boutin, A. Alchemical Osmostat for Monte Carlo Simulation: Sampling Aqueous Electrolyte Solution in Open Systems. *J. Phys. Chem. B* **2023**,

(56) Nilmeier, J. P.; Crooks, G. E.; Minh, D. D.; Chodera, J. D. Nonequilibrium candidate Monte Carlo is an efficient tool for equilibrium simulation. *Proc. Nat. Acad. Sci.* **2011**, *108*, E1009–E1018.

(57) Ross, G. A.; Rustenburg, A. S.; Grinaway, P. B.; Fass, J.; Chodera, J. D. Biomolecular simulations under realistic macroscopic salt conditions. *J. Phys. Chem. B* **2018**, *122*, 5466–5486.

(58) Astafan, A.; Bellat, J.-P.; Bezverkhyy, I.; Chaplais, G.; Daou, T. J.; Dirand, C.; Nouali, H.; Ryzhikov, A. 2023; Private communication, Experimental intrusion pressure of electrolyte solution in zeosils.

(59) Database of Zeolite Structures. 2023; Available online : , `http://www.iza-structure.org`.

(60) Olson, D.; Kokotailo, G.; Lawton, S.; Meier, W. Crystal structure and structure-related properties of ZSM-5. *J. Phys. Chem.* **1981**, *85*, 2238–2243.

(61) Calligaris, M.; Nardin, G.; Randaccio, L. Cation site location in hydrated chabazites. Crystal structure of potassium-and silver-exchanged chabazites. *Zeolites* **1983**, *3*, 205–208.

(62) Hriljac, J.; Eddy, M.; Cheetham, A.; Donohue, J.; Ray, G. Powder neutron diffraction and 29Si MAS NMR studies of siliceous zeolite-Y. *J. Solid State Chem.* **1993**, *106*, 66–72.

(63) Desbiens, N.; Demachy, I.; Fuchs, A. H.; Kirsch-Rodeschini, H.; Soulard, M.; Patarin, J. Water condensation in hydrophobic nanopores. *Angew. Chem. Int. Ed.* **2005**, *44*, 5310–5313.

(64) Jorgensen, W. L.; Chandrasekhar, J.; Madura, J. D.; Impey, R. W.; Klein, M. L. Comparison of simple potential functions for simulating liquid water. *J. Chem. Phys.* **1983**, *79*, 926–935.

(65) Chowdhuri, S.; Chandra, A. Hydration structure and diffusion of ions in supercooled water: Ion size effects. *J. Chem. Phys.* **2003**, *118*, 9719–9725.

(66) Mamatkulov, S.; Fyta, M.; Netz, R. R. Force fields for divalent cations based on single-ion and ion-pair properties. *J. Chem. Phys.* **2013**, *138*, 024505.

(67) Dubbeldam, D.; Calero, S.; Ellis, D. E.; Snurr, R. Q. RASPA: molecular simulation software for adsorption and diffusion in flexible nanoporous materials. *Mol. Simul.* **2016**, *42*, 81–101.

(68) Berendsen, H. J.; van der Spoel, D.; van Drunen, R. GROMACS: A message-passing parallel molecular dynamics implementation. *Comput. Phys. Commun.* **1995**, *91*, 43–56.

(69) Cailliez, F.; Boutin, A.; Demachy, I.; Fuchs, A. H. Thermodynamic study of water confinement in hydrophobic zeolites by Monte Carlo simulations. *Mol. Simul.* **2009**, *35*, 24–30.

(70) Washburn, E. W. The dynamics of capillary flow. *Phys. Rev.* **1921**, *17*, 273.

(71) Ortiz, A. Étude par simulation moléculaire de la flexibilité des matériaux nanoporeux: propriétés structurales, mécaniques et thermodynamiques. Ph.D. thesis, Université Pierre et Marie Curie-Paris VI, 2014.

(72) Porcheron, F.; Monson, P.; Thommes, M. Modeling mercury porosimetry using statistical mechanics. *Langmuir* **2004**, *20*, 6482–6489.

(73) Chempath, S.; Denayer, J. F.; De Meyer, K. M.; Baron, G. V.; Snurr, R. Q. Adsorption of liquid-phase alkane mixtures in silicalite: simulations and experiment. *Langmuir* **2004**, *20*, 150–156.

(74) Perego, C.; Giberti, F.; Parrinello, M. Chemical potential calculations in dense liquids using metadynamics. *Eur. Phys. J. Spec. Top.* **2016**, *225*, 1621–1628.

(75) Gates, J. A.; Wood, R. H. Densities of aqueous solutions of sodium chloride, magnesium chloride, potassium chloride, sodium bromide, lithium chloride, and calcium chloride from 0.05 to 5.0 mol kg-1 and 0.1013 to 40 MPa at 298.15 K. *Journal of Chemical and Engineering Data* **1985**, *30*, 44–49.

(76) Frenkel, D.; Smit, B. *Understanding molecular simulation: from algorithms to applications*; Elsevier, 2001; Vol. 1.

(77) Perez Sirkin, Y. A.; Factorovich, M. H.; Molinero, V.; Scherlis, D. A. Vapor pressure of aqueous solutions of electrolytes reproduced with coarse-grained models without electrostatics. *J. Chem. Theory Comput.* **2016**, *12*, 2942–2949.

(78) Panagiotopoulos, A. Z.; Quirke, N.; Stapleton, M.; Tildesley, D. Phase equilibria by simulation in the Gibbs ensemble: alternative derivation, generalization and application to mixture and membrane equilibria. *Mol. Phys.* **1988**, *63*, 527–545.

(79) Panagiotopoulos, A. Z. Monte Carlo methods for phase equilibria of fluids. *J. Phys. Condens. Matter* **2000**, *12*, R25.

(80) Vorholz, J.; Harismiadis, V.; Panagiotopoulos, A. Z.; Rumpf, B.; Maurer, G. Molecular simulation of the solubility of carbon dioxide in aqueous solutions of sodium chloride. *Fluid Phase Equilib.* **2004**, *226*, 237–250.

(81) Factorovich, M. H.; Molinero, V.; Scherlis, D. A. A simple grand canonical approach to compute the vapor pressure of bulk and finite size systems. *J. Chem. Phys.* **2014**, *140*, 064111.

(82) Abbas, Z.; Ahlberg, E. Activity coefficients of concentrated salt solutions: A Monte Carlo investigation. *J. Solut. Chem.* **2019**, *48*, 1222–1243.

(83) Bockris, J. O.; Reddy, A. K.; Gamboa-Aldeco, M. E. *Modern electrochemistry 2B: electrodics in chemistry, engineering, biology and environmental science*; Springer Science & Business Media, 1998; Vol. 2.

(84) Guggenheim, E.; Turgeon, J. Specific interaction of ions. *Trans. Faraday Soc.* **1955**, *51*, 747–761.

(85) Ciavatta, L. The specific interaction theory in evaluating ionic equilibria. *Ann. Chim.(Rome)* **1980**, *70*, 551.

(86) Bromley, L. A. Thermodynamic properties of strong electrolytes in aqueous solutions. *AIChE journal* **1973**, *19*, 313–320.

(87) Pitzer, K. S.; Press, C. *Activity coefficients in electrolyte solutions*; CRC press Boca Raton, FL, 1991; Vol. 2.

(88) Kim, H. T.; Frederick Jr, W. J. Evaluation of Pitzer ion interaction parameters of aqueous mixed electrolyte solutions at 25 °C. 2. Ternary mixing parameters. *J. Chem. Eng. Data* **1988**, *33*, 278–283.

(89) Kim, H. T.; Frederick Jr, W. J. Evaluation of Pitzer ion interaction parameters of

aqueous electrolytes at 25 °C. 1. Single salt parameters. *J. Chem. Eng. Data* **1988**, *33*, 177–184.

(90) Fernández-Mérida, L.; Rodríguez-Raposo, R.; García-García, G. E.; Esteso, M. A. Modification of the Pitzer equations for application to electrolyte+ polar non-electrolyte mixtures. *J. Electroanal. Chem.* **1994**, *379*, 63–69.

(91) Simoes, M. C.; Hughes, K. J.; Ingham, D. B.; Ma, L.; Pourkashanian, M. Estimation of the Pitzer Parameters for 1–1, 2–1, 3–1, 4–1, and 2–2 Single Electrolytes at 25 °C. *J. Chem. Eng. Data* **2016**, *61*, 2536–2554.

(92) Humphreys, M. P.; Schiller, A. J. Pytzer: the Pitzer model for chemical activities and equilibria in aqueous solutions in Python (beta). **2021**,

TOC Graphic

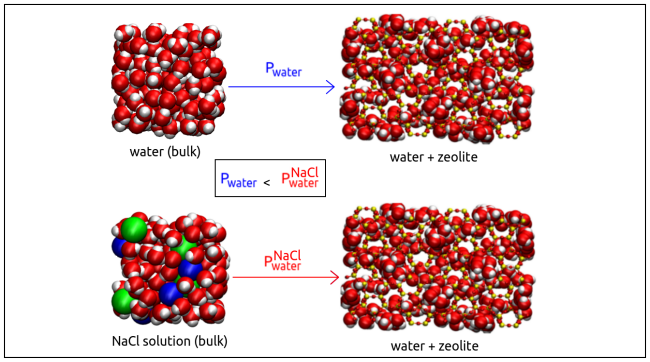
P water
water (bulk)
water + zeolite
P water < P NaCl water
P NaCl water
NaCl solution (bulk)
water + zeolite